JOURNAL OF MATERIALS SCIENCE 28 (1993) 6136–6146

Strengthening of alloy 8090 and its fracture mechanics parameters

Z. BURZIĆ, J. ČUROVIĆ
The Aeronautical Institute, Žarkovo-Belgrade, Yugoslavia
N. GRAHOVAC, V. M. STEFANOVIĆ
The Institute of Nuclear Science, Vincha-Belgrade, Yugoslavia

An investigation has been made of the tensile properties, impact-, initial fracture toughness and fracture mode of an aluminium–lithium 8090 alloy at room temperature and 77 K, depending upon the heat treatment and orientation. The peak-aged material exhibited an excellent combination of strength and toughness, equal to or exceeding that shown by the high-strength aluminium alloys of the 2000 and 7000 series. The superior strength and toughness of peak-aged plates, including that of 3% stretched material, compared to underaged material seems to be associated with the lower content of coarse insoluble precipitates, a higher density of S′-precipitates in a matrix ligament (grain) which promote ductile fracture. The impact toughness of the peak-aged specimens increased at 77 K only in the L–T plate orientation, while in the T–L orientation it was somewhat lower or remained the same. The toughness increase at 77 K is discussed in terms of the role of the matrix and (sub)grain-boundary precipitates, freezing of low-melting point impurities of sodium and potassium alkaline metals at (sub)grain boundaries and the occurrence of the fine crack divider delamination toughening. The yield strength, $R_{0.2}$, increase on ageing was accompanied by a corresponding increase in initial crack divider fracture toughness, K_{Ic}, opposite to the trends obtained for some traditional high-strength aluminium alloys. Changes of K_{Ic} versus $R_{0.2}$ depending on orientation are discussed using models for ductile fracture toughness behaviour of aluminium alloys, based on the criterion that a critical width of the heavily strained zone at the crack tip approximates the average ligament width, d_p, i.e. the thickness of the elongated grain in the L–T and T–L plate orientations. It was also found that, for constant chemical composition and fabrication practice of the alloy, a critical plate thickness exists $B \approx 0.16\ t_i$, where t_i is the initial thickness of the rolling ingot, for which the tensile strength properties in the L–T orientation are the same as that in the T–L orientation, while the plasticity (measured by elongation to failure) of the plate is a maximum. Two types of laminated cracks were observed on fracture surfaces of the specimens: large, >1 mm deep (the number of these cracks remains the same as the number of hot-rolling passes), and fine <0.4 mm (shallow laminated cracks, the number of which significantly increases with decreasing temperature, 77 K).

1. Introduction

Over the past two decades, high-strength lithium-containing aluminium alloys have been the subject of considerable widespread interest of many aerospace airframe designers, owing to their improved specific strength, low density, high elastic modulus, acceptable fracture toughness, damage tolerance and the good resistance to fracture initiation and fatigue crack propagation. The alloys are used for the newer generation sub-, super-, hypersonic aircraft lightweight structures, such as for advanced tactical fighters and civil aircraft. Prominent among these alloys is the 8090 alloy for medium-strength replacement of traditional aluminium alloys, and carbon-fibre composites. The influence of composition, purity and thermomechanical heat treatment on microstructure and mechanical properties of these alloys is widely presented in the literature [1–7]; however, much more data on the performance of these highly anisotropic materials is needed for a full application. A detailed understanding of the microstructural mechanisms that accurately describe the strength and toughness of wrought products is also not completely clear [8–11].

Thus, the purpose of the present study was to examine mechanical properties, toughness levels and fracture behaviour of 8090 alloy plates at room temperature and 77 K, comparing them to commercial 8090 and the other high-strength aluminium alloys. Tensile-, impact- and fracture toughness properties have been determined in aged, a two-step aged,

0022–2461

stretched and aged conditions, depending on orientation. The fracture modes associated with tensile, impact and compact (tension) specimens were also examined.

In particular, the dependence of fracture toughness, K_{Ic}, on yield strength and orientation was considered by the application of the present critical crack-tip opening displacement models for ductile fracture [12, 13].

2. Experimental procedure

Ingots of the pure alloy 8090, produced by the Institute at Vincha [14], were hot rolled to 6 and 10 mm thick plates with the actual composition and density given in Table I. Ingots were prepared in 16 kg heats by induction melting of pure metals and master alloys under vacuum (degassing). Lithium packed in special aluminium capsules was added into a spinel-coated graphite crucible under high-purity argon (0.6 atm) followed by casting into a permanent steel mould. Small ingots, up to 2 kg mass, were also cast into ceramic moulds. Details of the casting process will be published elsewhere [14]. The original cast ingots were homogenized in air in two steps: heated at 753 K, for 3.7 h followed by 803 K, 3.7 h, water quenched and then the surface layer was scalped off to 38 mm thickness. After preheating at 773 K and finishing at 623 K the ingots were hot rolled into plates to a final thickness. The hot rolling was performed in five steps with intermediate reheating between passes. A series of specimen blanks was taken from the plate in the L–T and T–L orientations. After solution heat treating, the blanks were aged to obtain two levels of strength: under-aged (UA) and peak-aged (PA). The following heat treatment procedures for blanks were used: (a) solution heat treatment at 793 K in air for 1/2 h (SHT), water quenching (WQ), natural ageing (NA) for a month and final artificial ageing (FAA) at 441 K for 8 h (temper T6-VA) or FAA at 463 K for 16 h (temper T6-PA); (b) SHT + WQ followed by a 3%–4% permanent tensile strain to simulate the stretching process, NA and FAA at 441 K, 8 h (temper T8-UA) or FAA at 463 K, 16 h (temper T8-PA). All specimen blanks were solution treated and aged between two massive copper plates heated in air for different periods of time.

Tensile tests were performed on round or square specimens machined from the blanks with the cross-sectional area of 80 and 100 mm^2 and 25 mm gauge length, respectively.

The impact toughness was measured on the L–T and T–L Charpy V-notch standard specimens at room temperature and 77 K. The notch was cut in the thickness direction (S) so that crack extension is in the transverse (T) or longitudinal (L) direction. Tests were carried out using a computer-aided instrumented Charpy impact testing system Schenck, ~100 kN, under an impact velocity of 5 ms^{-1}. The specimens were fractured after 1/12 h immersion in liquid nitrogen to attain 77 K.

Initiation fracture toughness tests were conducted on 10 mm thick fatigue precracked compact tension, C(T) samples (Fig. 1), machined in the same directions as tensile and impact specimens. The elastic–plastic fracture toughness integral, J_{Ic}, was obtained, because the requirements for "valid" plane strain conditions, B (thickness) $\geq 2.5\ (K_{Ic}/R_{0.2})^2$ cannot be met in these samples for T6-UA and T6-PA tempers examined. The area under the load–crack opening displacement plots, after initiation, was taken to represent the total energy required to propagate the crack. A 5% secant offset procedure of one C(T) sample was used to determine the critical load required to estimate J_{Ic} values. Tests were conducted in laboratory air, RH ≈ 65%. From such J_{Ic} energies, K_{Ic} values were then derived using the equation

$$K_{Ic} \approx (E'J_{Ic})^{1/2} \quad (1)$$

where E' is the Young's modulus, E, in plane stress, and $E/(1-\nu)^2$ in plane strain, ν is Poisson's ratio; $\nu = 0.31$ here, determined for the 8090 alloy. Further details are given in ASTM E-399 and E-183 standards.

The work-hardening exponent, n, was obtained by calculation from the load–elongation curves, assuming that the relationship $R = \text{const}\ \varepsilon^n$ after 0.2% offset plastic strain, is valid.

The microstructures and fracture surfaces of all specimens were examined as usual, using optical and scanning electron microscopy (SEM).

TABLE I Composition and density of alloy 8090[a]

Composition (mass %)								Density ($kg\,m^{-3}$)
Li	Cu	Mg	Zr	Ti	Fe	Si	Al	
2.48	1.33	0.67	0.12	0.07	0.02	0.03	Bal.	2535

[a] Fe, Si are impurities; Cu/Mg = 2.

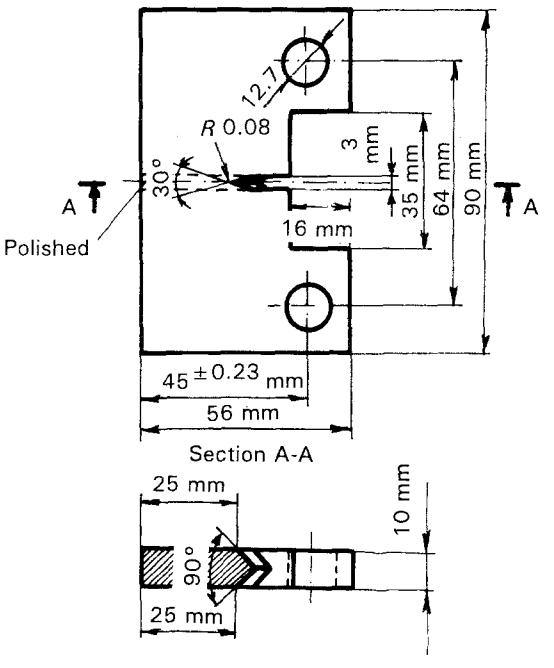

Figure 1 Compact tension test specimen for J_{Ic} determination (W = 45 mm).

3. Results and discussion

3.1. Microstructures

The microstructures of 8090 alloy is strongly dependent on the solidification rate of the ingot, volume fraction of insoluble particles and fabrication practice.

Microstructure of the slowly cooled ingot 8090 alloy is shown in Fig. 2a–c. The as-cast microstructure, cooling rate $\approx 0.125\ K\ s^{-1}$, consists of large equiaxed grains with an unusual thick layer of continuously distributed intermetallic phases precipitated along the grain boundaries, Fig. 2a. The light-etching grain-boundary phases were identified by X-ray diffraction and SEM as equilibrium δ (LiAl), S (Al_2CuMg) and T (Cu, Li)-rich phases of the eutectic temperature 816 K [14]. The dark-etching fields observed along grain boundaries are pores created during metllographic preparation of specimens, because the etching solution selectively attacks the lithium-rich coarse constituents. After high-temperature homogenization, the intermetallic phases were fully dissolved so that the only insoluble intermediate zirconium-bearing particles β′ (Al_3Zr) remained in the microstructure. In addition to these dispersoids, prolonged NA after WQ resulted in the formation of large ordered "domains" of the δ′ (Al_3Li) phase throughout the grain, Fig. 2b. The artificial ageing at 463 K, 17 h, further transforms the preceding microstructure; ordered domains disappear and instead of them a network of the S and T precipitates is formed with the simultaneous reprecipitation of coarse particles at grain boundaries. The appearance of this precipitate network on the polished and etched surface of the specimens depends on grain orientation; sometimes it looks like cells (arrowed in Fig. 2c). Higher cooling rates were desirable to reduce larger amounts of the soluble grain-boundary phases, shown in Fig. 2a. The steel-mould casting produces an ingot with fine-grained microstructure and smaller amounts of the precipitated phases, mainly distributed at the triple-point grain boundaries. After homogenization and quenching, these δ and T grain-boundary phases were completely dissolved into the matrix, except that of β′ dispersoids. Further microstructural refining of the rapidly cooled ingots can be achieved by a combination of hot and cold working of the homogenized ingot. A series of microstructures were obtained after heat treatment, examples are shown in Fig. 3 and later in Fig. 5. Fig. 3a and b reveal a predominantly unrecrystallized anisotropic grain microstructure of the as-hot rolled and PA 10 mm thick plates with typical "pancake"-shaped grains flattened and elongated in the rolling direction (L). The grains of the 10 mm thick

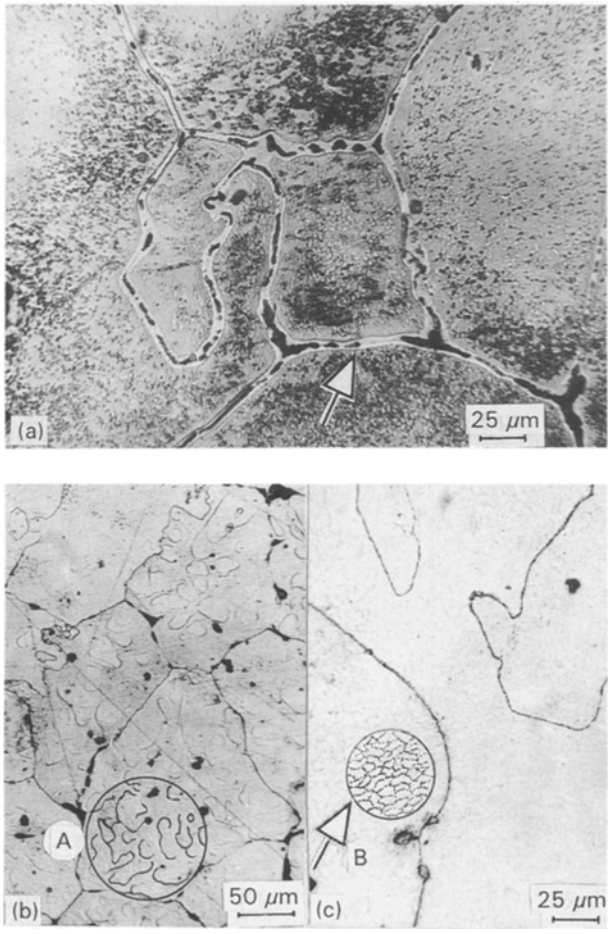

Figure 2 Optical micrographs of the microstructure of 8090 alloy slowly solidified in a ceramic mould ($\approx 0.125\ K\ s^{-1}$): (a) as-cast, showing a thick layer of precipitated phase at grain boundaries; (b) as-quenched and NA, ordered "domains" of δ′ phase (A); (c) WQ + NA and FAA at 463 K, arrow shows coarse precipitates in the matrix (B).

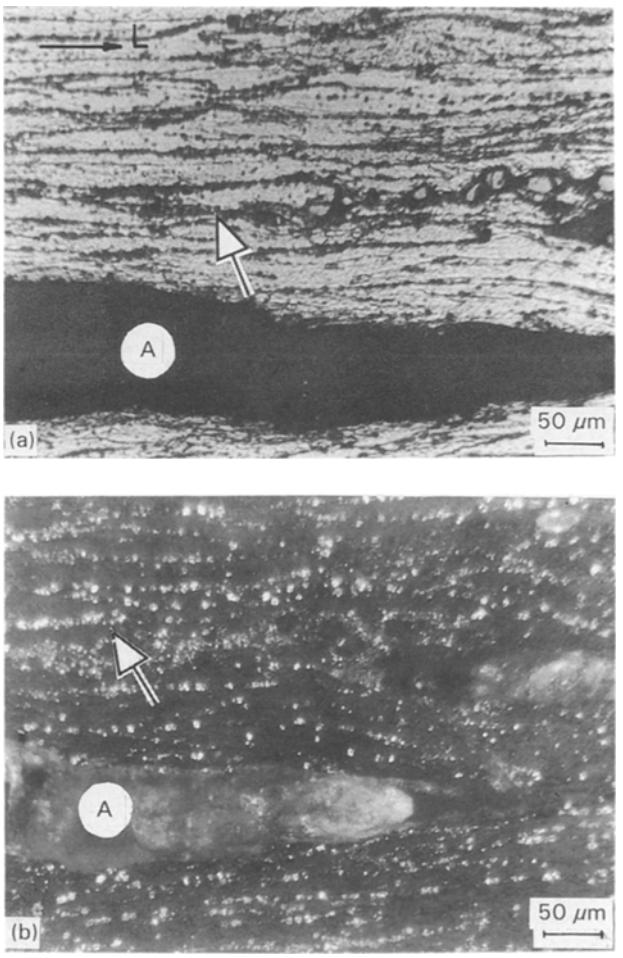

Figure 3 Optical micrographs of the microstructure of peak-aged Charpy specimens around a large laminated crack (A): (a) the grain-boundary precipitates, S, T, β′-white light; (b) the same position under polarized light.

plates are roughly 20–40 μm thick, 100–150 μm wide and 0.1–1 mm long and the aspect ratio is ≈1:25. In the T6-PA condition, high-angle grain boundaries were decorated with a high density of particles, β′ dispersoids and constituent coarse S and T precipitates, which favour intergranular delamination of the plate materials. The volume fraction of these precipitates increases with ageing up to the peak-aged condition, T6 (T8)-PA tempers. The widespread grain-boundary precipitates of the T6-PA specimens are evident in Fig. 3a and b.

The microstructural phases with the most important influence on properties, particularly strength and toughness in the alloy plates are of three types: (a) the soluble equilibrium δ, S and T-type copper- and magnesium-rich phases continuously distributed along grain boundaries as a thick layer or coarse precipitates; (b) the insoluble intermediate size zirconium bearing cubic particles, known as β′-dispersoids, localized at grain boundaries with the greatest influence in the formation of a strong rolling texture, and (c) the primary strengthening spherical, ordered, coherent δ′ matrix precipitates and S′-laths predominantly nucleated on dislocations [15]. Grain-boundary precipitation in this alloy appears to be largely suppressed by prolonged NA and cold deformation which accelerates the nucleation of S′-laths on network dislocations.

3.2. Tensile properties

Uniaxial tensile property data of the material in the as-cast, hot-rolled and aged conditions are listed in Table II. It can be clearly seen that the variations in strength and ductility are on a wide scale, depending on fabrication practice and resulting microstructure. Very low strength and elongation to failure were found in as-cast, slowly solidified material ($0.125\ K\ s^{-1}$). The microstructural features responsible for such a low-strength and ductility are coarse grain size and continuously precipitated second-phase particles at grain boundaries (see Fig. 2a). The tensile properties of homogenized, WQ and NA material, however, are significantly improved by a factor of 2, due to a homogeneously precipitated δ′ phase, but following final artificial ageing at 463 K the effect of precipitation is quite large, resulting in a repeated substantial decrease in strength to an extremely low value of only 31.2 MPa. Such a dramatic decrease in strength is attributed to arise from the nearly complete precipitation of alloying atoms and thus a high volume fraction of the coarse non-strengthening δ, S and T-type precipitates in the grain matrix or at grain boundaries.

In its rapidly cooled form, the alloy was superior to the slowly solidified material. Tensile strength increases by a factor of 2.5, while the non-uniformly precipitated phases and super-saturated solid solution give completely brittle material for further processing. Considerable improvement in tensile properties, especially in elongation to failure, are achieved during hot rolling of the homogenized ingot by the removal of the excess amounts of the soluble grain-boundary phases. The elongation to failure of the as-hot-rolled plates

TABLE II Room-temperature tensile properties of Vincha aluminium–lithium pure alloy 8090 in as-cast and artificially aged conditions, compared with commercial 8090 and conventional alloys. Strain rate $4.2 \times 10^{-4}\ s^{-1}$, Pisson's ratio, $\nu = 0.31$

Material, ageing treatment	Elastic modulus, E (tensile) (GPa)		Yield strength, $R_{0.2}$ (MPa)		Ultimate tensile strength, R_m (MPa)		Elongation A (%) (on 25 mm)		Strain-hardening exponent, n		Notes, reference
	L–T	T–L	L–T	T–L	L–T	T–L	L–T	T–L	L–T	T–L	
As cast CM[a]	–	–	–	–	100.0		2.5		–	–	Cooling rate ≈ 7.5K min^{-1}
Hom., WQ + NA	–	–	–	–	205.0		4.4		–	–	
aged at 463 K	–	–	–	–	31.2		2.3		–	–	Brittle
As-cast SM[b]	–	–	–	–	240.0		0.3		–	–	Brittle
As-hot-rolled 10 mm plates	–	–	183.5	–	279.9	–	13.4	–	–	–	Ductile
T6-UA, 10 mm	75.9	75.3	327.9	322.4	444.1	421.6	7.0	4.0	0.11	0.11	–
T8-UA, 10 mm	83.3	81.2	377.7	449.5	459.1	455.3	7.0	4.6	0.11	–	–
T8-UA, 6 mm	–	–	432.8	430.0	496.1	495.3	11.6	11.6	–	–	Ductile, necking
T6-PA, 10 mm	81.8	78.8	389.4	369.5	477.3	416.3	6.5	3.4	0.10	0.13	–
T8-PA, 10 mm	85.0	80.6	426.5	423.1	494.5	445.2	6.0	2.4	–	–	
T8-PA, 6 mm	–	79.3	467.5	455.0	518.8	510.7	12.1	11.1	–	–	Ductile, necking
8090-T851, 12 mm	81.0	–	455.0	–	500.0	–	7.0	–	–	–	[12]
8090-T8X, 11–16 mm	–	–	482.0	–	534.0	–	6.1	–	0.08	–	[11]
7150-T651	–	–	404.0	–	480.0	–	6.0	–	–	–	[11]
2024-T851	72.0	–	450.0	–	485.0	–	6.0	–	–	–	[22]

[a] CM = ceramic mould

[b] SM = steel mould; a minimum of three specimens was tested for each condition, no significant variation between the specimens was observed.

increase markedly up to 13.4%. These features were controlled by the starting thickness of the ingot, number of passes, total rolling reduction, processing temperature and the final TMT to obtain two levels of strength in T6 and T8 tempers. Prolonged NA and FAA to T6-PA temper results in an increase in strength with a concurrent reduction in ductility. The effect of stretching was fairly modest, i.e. it increases the strength without any detriment to elongation in the L–T orientation. Cold stretching 3%–4% after solution treatment increases the strength whereas the ductility remained approximately 6%–7% and 2.4%–4.6% in the L–T and T–L orientations, respectively. For 10 mm thick plates, the yield and tensile strengths are 5%–10% lower in the T–L orientation that the corresponding values in the L–T orientation, whereas elongation to failure shows the larger decrease, 50%–150% in the T–L orientation. The application of higher hot-rolling reductions was seen to improve the strength and particularly ductility. Compared to 10 mm thick material, the yield and tensile strengths of 6 mm thick plate were up to 10% higher, while elongation to failure values were 102%–360% higher in the L–T and T–L orientations, respectively. The specimens cut from 6 mm thick plates failed with evidence of small localized necking before final failure, see Fig. 4. Nearly the same values of tensile properties in both orientations, L–T and T–L, were obtained. It can be clearly seen, that a starting thickness of the rolling ingot plays a large part in determining the L–T and T–L tensile properties of the alloy plane semiproducts (plates, sheets). Considering strength and ductility, a critical thickness of the rolling product exists, B_c, for which the L–T and T–L tensile properties are the same

$$B_c \approx 0.16 t_i, \qquad (2)$$

where t_i is a starting thickness of the rolling ingot. The relationship is valid for a constant composition, i.e. dispersoid content of the alloy and unchangeable casting and fabrication practices. For $t_i = 38$ mm thick rolling ingot, in the present study, there is a critical plate thickness of $B_c = 6$ mm. It was observed that the transition in deformation mode occurs in the L–T and T–L orientations with a decrease in the thickness of semiproducts. After rolling to 1.6 mm thick unrecrystallized sheet, however, extremely low elongation to failure values of only 2%–3% were obtained in the L–T orientation [16, 17], so that an orientation dependence of elongation to failure and thickness exists. A reason for this behaviour is discussed in the last section.

Tensile properties of the pure 8090 alloy can be compared with commercial 8090 and traditional aluminium alloys 7150 and 2024 series (Table II).

Typical stress–strain curves for the as-cast and heat-treated materials are shown in Fig. 4. According to the strengthening mechanism proposed by Miller *et al.* [18], a possible contribution of strengthening components to the shear yield stress, τ_y, of the alloy 8090 is predicted by the equation

$$\tau_y = \tau_{SS} + \tau_{\beta'} + \tau_B + \tau_{\delta'} + \tau_{S'} + \cdots \qquad (3)$$

where τ_{SS} is strengthening from lithium, copper and magnesium atoms in solid solution; $\tau_{\beta'}$, $\tau_{\delta'}$ and τ_S are strengthening due to the presence of β′ dispersoids, δ′ and S′ precipitates, respectively. τ_B is strengthening

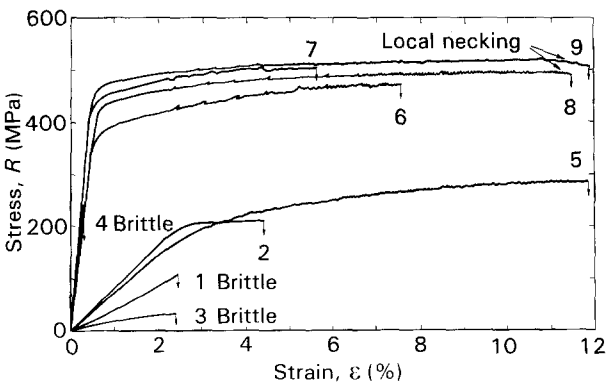

Figure 4 Typical stress–strain curves of 8090 alloy at room temperature in: (1) as-cast CM ($\approx 0.125\ K\,s^{-1}$); (2) CM cast + hom. + WQ + NA; (3) CM cast + WQ + NA + FAA; (4) as-cast SM; (5) SM cast + hom. and as-hot-rolled in the L–T orientation; (6) 10 mm plates in T8-UA, L–T orientation; (7) 10 mm plates in T8-PA, L–T orientation; (8) 6 mm plates in T8-UA, L–T orientation; (9) 6 mm plates in T8-PA, L–T orientation.

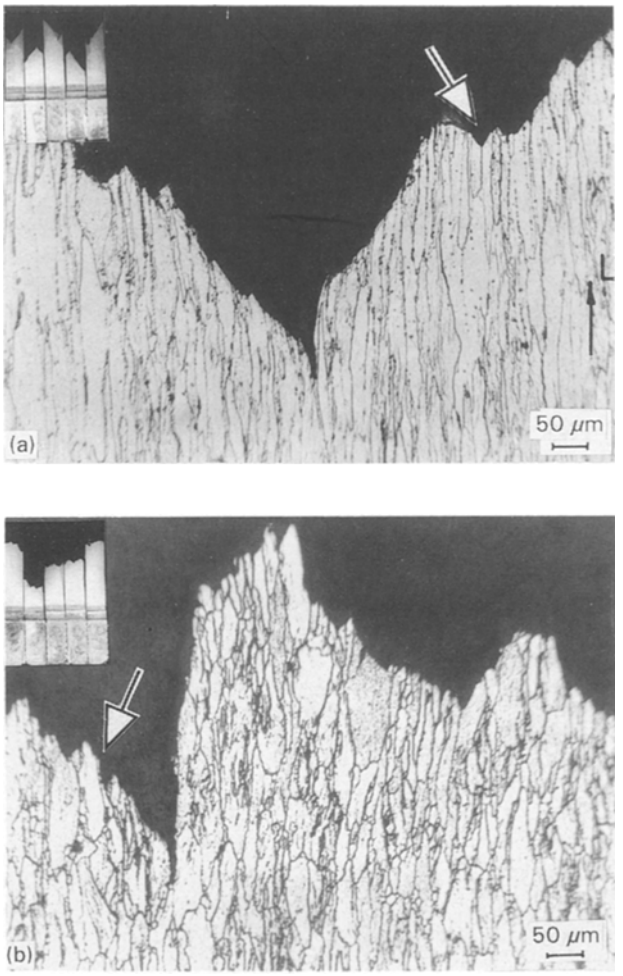

Figure 5 Optical micrographs of the tensile specimen fracture modes at room temperature. Arrows show: (a) T6-UA condition, transgranular shear in the L–T, and (b) T6–PA, inter(sub)granular fracture in the T–L orientation.

from dislocation substructure and (sub)grain boundaries. In the as-cast and heat-treated microstructures the main contributions to strengthening are: Curve (1) from $\tau_{\beta'} + \tau_{SS}$; Curve (2) $\tau_{\beta'} + \tau_{SS} + \tau_{\delta}$; Curve (3) from $\tau_{\beta'}$ only; Curve (4) $\tau_{SS} + \tau_{\beta'}$. In the as-hot-rolled microstructure Curve (5) strengthening results from $\tau_B + \tau_{SS} + \tau_{\beta'} + \tau_{\delta'}$. In the stretched and aged T6 and T8 tempers, Curves (6–9), a strong dislocation interaction with S′ precipitates exists [15] and highest strength levels are attained due to $\tau_{S'} + \tau_{SS} + \tau_{\delta'} + \tau_{\beta'} + \tau_B$. Other coarse, δ, S and T-type precipitates predominantly distributed at grain boundaries do not contribute to strength.

The fracture mode of the tensile specimens at room temperature is illustrated in Fig. 5a and b. On the macroscopic scale, the L–T tensile specimens in T6-UA temper failed predominantly by transgranular shear at $\approx 45°$ to the rolling-tensile axis, while with the T6-PA specimens in the T–L orientation fracture is inter(sub)granular in nature. Some degree of splitting is also observed at room temperature.

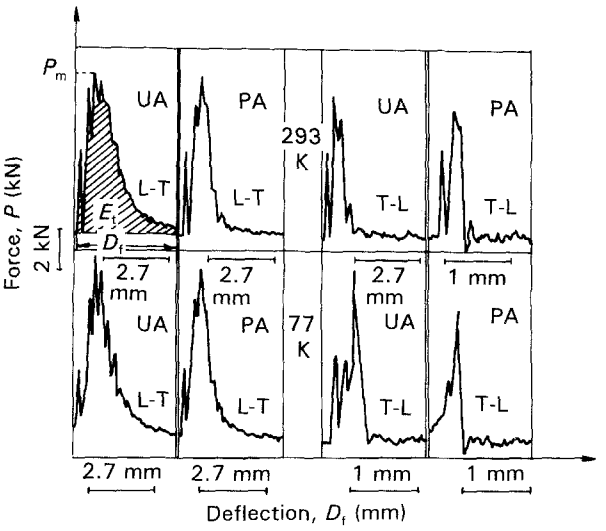

Figure 6 Typical force–deflection curves of Charpy impact specimens in the T6-UA and T6-PA conditions tested at room and cryogenic temperature (77 K).

3.3. Charpy impact toughness

The crack-divider impact toughness data of Charpy specimens at room (293 K) and liquid nitrogen temperature (77 K) are shown in Table III. The total impact-absorbed energy, expressed by the impact toughness, R_0, of the T6-UA plate in the L–T orientation is up to 60% higher, than for T6-PA plate material in the T–L orientation. At 77 K, the L–T toughness of the PA specimens increases significantly to more than 50%. Maximum load, P_m, and deflection until fracture, D_f, values in the L–T specimens also show a significant enhancement at 77 K compared to 293 K. These findings are in agreement to that reported by Kabayashi *et al.* [8]. However, the corresponding R_0 values of 10 mm thick plates in the T–L orientation show a decrease of more than 30% at 77 K as low as those at 293 K. The T–L toughness decrease is found to be more strongly dependent on the lower D_f at 77 K, because of the increased tendency to intergranular laminated fracture. The force–deflection (P–D) curves of the T–L specimens show whole brittle fracture behaviour at both temperatures, see Fig. 6. The increases in R_0 at 77 K are considered to be caused mainly by the increases in P_m as well as D_f, depending also on various shapes of the P–D curves. It is also found that the number of high peaks on the P–D curves is approximately equal to the number of large laminated cracks observed on the fracture surface of specimens. Such results are inconsistent with many published explanations, which relate the low-temperature increase in L–T impact toughness solely to the solidification of (sub)grain-boundary fusible phases resulting in slip homogeneity and higher ductility [19–21].

Two types of laminated cracks on the fracture surface of specimens were observed: large (LLC), 1–2 mm, and fine (FLC), shallow, 0.1–0.4 mm in depth. The LLC are parallel to the rolling plane and perpendicular to the fracture surface of the specimen, see Figs 7a and b and 8a and b. The fracture surfaces of these cracks are decorated by a number of particles, intermediate β′ and coarse S and T (copper, magnesium, lithium)-rich precipitates (Fig. 3), formed during hot- and finished rolling. Coarse precipitates are difficult to remove during the solution treatment and remain elongated with the grains to give a plate fibrous structure. Fractures of UA specimens rarely show evidence of high-angle grain-boundary precipitates; the grain boundaries are thus comparatively more resistant to delamination cracking so that the impact

TABLE III Charpy impact toughness, R_0 of 10 mm thick 8090 alloy plates, in underaged and peak-aged conditions at room temperature and 77 K

Temper	Orientation	Charpy impact toughness, R_0 (kJ m^{-2})			Maximum force, P_m (kN)		Deflection, D_f (mm)		Reference
		293 K	77 K	% change	293 K	77 K	293 K	77 K	
T6-UA	L–T	128.0	129.2	+1.0	8.8	9.7	2.8	2.9	This work
T6-UA	L–T	22.7	26.2	+ 15.4	1.3	1.5	0.8	0.9	6 mm plates [8]
T6-PA	L–T	62.0	95.0	+ 53.0	8.4	8.9	1.6	2.0	This work
T6-PA	L–T	18.7	23.7	+ 26.7	1.5	1.6	0.7	0.8	6 mm plates [8]
T6-UA	T–L	48.0	33.0	− 31.2	7.2	8.7	1.0	0.8	This work
T6-PA	T–L	41.0	36.0	− 12.0	6.1	7.5	0.6	0.6	This work

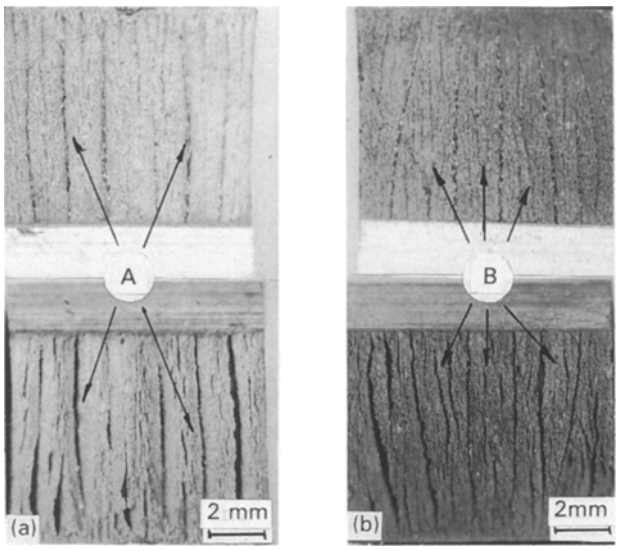

Figure 7 Optical micrographs of the Charpy impact specimens fracture at (a) room temperature, LLC (A); (b) 77 K, FLC (B).

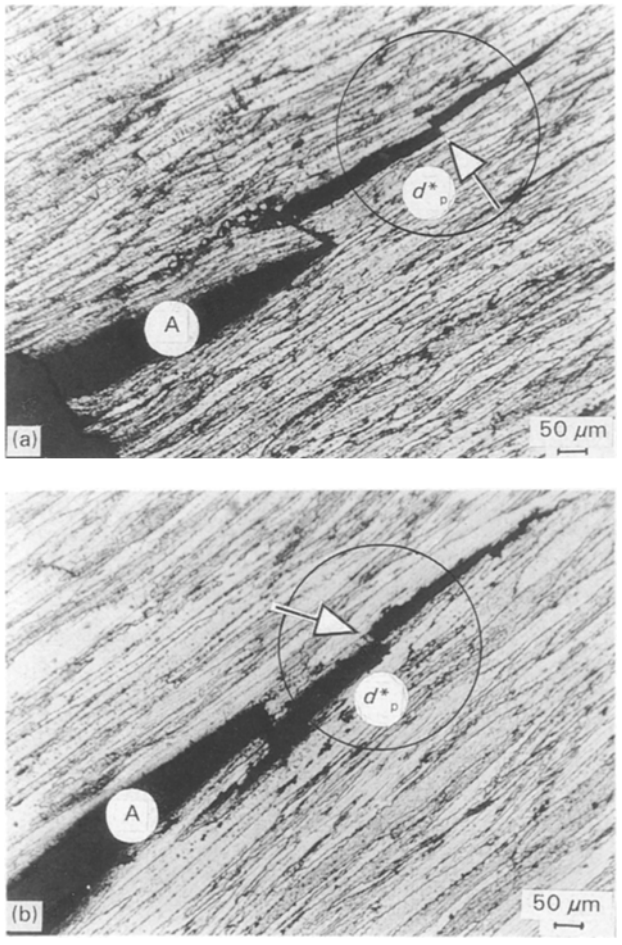

Figure 8 Optical micrographs of the peak-aged microstructure of Charpy impact specimens showing fracture mechanism at 293 and 77 K in the vicinity of a large laminated crack (A): (a) inter(sub)granular fracture. Arrow shows broken ligament, d^*_p, at 293 K; (b) transgranular shear fracture of plastic ligament at 77 K (the same mechanism as in C(T)-UA samples at 293 K). The fracture plane of the main crack is normal to the photograph.

toughness does not increase markedly at 77 K. The second type, FLC were found to follow the longitudinal and also transverse direction of the specimens. The cracking at grain and subgrain boundaries is predominant with decreasing temperature and is created by the increase in the critical resolved shear-stress component for slip into the matrix of a ligament (grain). It is apparent that a single delamination spacing and depth of FLC is difficult to determine, because a distribution of delaminations exists with several fine splits in between the LLC. The FLC are usually cracked after fracture of a few adjacent ligaments by inter(sub)granular or transgranular shear. The number of the FLC is two to three times greater at 77 K than 293 K, Figs 7 and 9. Optical (Fig. 8) and SEM (Fig. 9) photographs of the peak-aged Charpy impact specimens show a fracture mechanism transition from inter(sub)granular to partly transgranular shear in nature with the appearance of a number of FLC at 77 K (Figs 7b and 9b). The increase in the number of FLC, an areal fraction, increases the work of fracture while promoting a plane-strain condition at the crack tip.

Several theories have been proposed for the increase in impact toughness of aluminium–lithium alloys at low-temperatures [10, 12, 13, 19, 22]. However, these theories do not explain why the toughening is specific to specimen orientations (L–T, T–L). The two most important theories are: firstly, related to the phenomenon of segregation of sodium- or potassium-rich low melting point impurity phases at (sub)grain boundaries during ageing [19]. The presence of these fusible phases has been detected by Auger spectroscopy as the

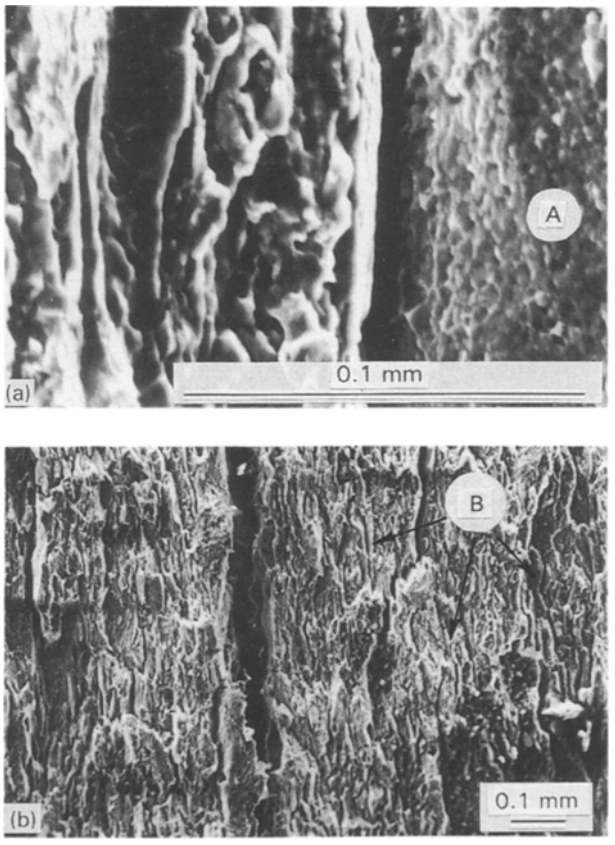

Figure 9 Scanning electron micrographs of the L–T Charpy impact specimens in the PA condition illustrating a fracture mechanism transition from (a) inter(sub)granular at 293, large crack (A), to (b) transgranular shear at 77 K. Arrows indicate the direction of the main crack advance on the fracture surface, fine cracks (B) (see also Fig. 7b).

sodium and potassium spectra [8]. Secondly, an alternative explanation has focused on the greater propensity of some aluminium alloys for through-thickness splitting normal to the fracture plane, along the weak interface elongated grain microstructure, known as the crack-divider delamination toughening [10, 12, 13, 22]. Crack-divider toughening in 8090 alloy plates can be achieved at 77 K in the L–T orientation by the relaxation in stress triaxiality and the resulting transformation of the global plane strain fracture into a series of local plane stress "thin sheet" failures due to formation of laminated cracks ahead of the crack tip [10, 22].

Based on the above, the changes of impact toughness of the T6-PA specimens at 77 K are possibly a result of the presence of both mechanisms. The increase in toughness at 77 K is associated with a distinct transition in the fracture mechanism from inter(sub)granular microvoid coalescence (293 K) to transligament (transgranular) shear. In fact, the increase of toughness of 8090 alloy plates comes from the freezing of (sub)grain-boundary fusible phases at 77 K, assuming that the suppression of the subgrain-boundary fracture is decisive in the L–T (where failures are partly subgranular), than in T–L specimens where the coarse high-angle grain-boundary particles have a predominant effect on toughness. Cracking at subgrain boundaries is more suppressed at 77 K because of an increased cohesion force at the subgrain/impurity (sodium, potassium) interface without coarse precipitates. An increase in impact toughness of the alloy is also accompanied by the formation of FLC at 77 K, although it is probably not the only reason for the increase. There is some conflicting evidence as to whether the extent of laminate crack formation, directionality and heat treatment improve toughness [8, 10, 22].

3.4. Initial crack-divider fracture toughness

The values of the initial crack-divider fracture toughness, K_{Ic}, (for plane strain condition) of 10 mm thick plates 8090 alloy at room temperature are shown in Table IV. Additionally, data for the tensile strength are listed in Table II. It is clearly apparent that the increases in yield strength, $R_{0.2}$ on FAA are accompanied by a considerable increase in K_{Ic}. The influence of orientation on toughness values can be seen to be about 15%–23% higher in the L–T compared to T–L orientation.

Micrographs of the fracture surfaces revealed a fracture mechanism of the UA and PA compact tension, C(T), samples at room temperatures (Fig. 10a and b; see also Fig. 8b). The fracture surface of the L–T samples in the temper T6-UA failed predominantly by transgranular shear, while T6-PA fracture inter-(sub)granularly.

The dependence of K_{Ic} on $R_{0.2}$ for different materials is shown in Fig. 11. The room-temperature K_{Ic} values are comparable with those shown by traditional high-strength aluminium alloys [9, 13, 23] and

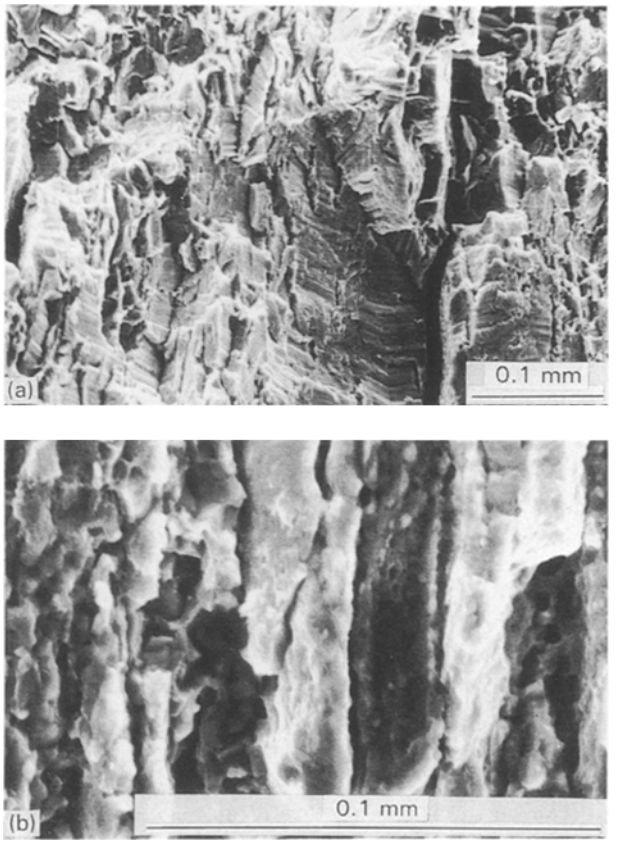

Figure 10 Scanning electron micrographs of the fracture surfaces of the C(T) samples at room temperature: (a) T6-UA, transgranular shear, and (b) T6-PA, inter(sub)granular (see also Fig. 8a).

TABLE IV Crack divider initial fracture toughness, K_{Ic}, ligament width, d_p calculated from Equation 3 and the ratio R_0/J_{Ic} of 8090 alloy plates 10 mm thick in the T6-UA and PA conditions at room temperature

Temper	Orientation	Fracture toughness K_{Ic} (MN/m$^{-3/2}$)	Initial energy, J_{Ic}, (kJ m^{-2})	Ligament width [a], d_p, (μm)	Ratio R_0/J_{Ic}, (Tables III and IV)	Reference
T6-UA	L–T	31.1	11.8	39	10.8	This work
T6-PA	L–T	36.0	14.6	41	4.5	This work
T6-UA	T–L	25.2	6.9	26	7.0	This work
T6-PA	T–L	30.5	10.2	32	4.0	This work
8090-T851	L–T	33.0	–	–	–	12 mm plates [18]
8090-T851	T–L	30.0	–	–	–	12 mm plates [18]
8090-T8X	L–T	36.0	–	–	–	11–16 mm plates [11]

[a] Measured $d_p \approx d = 20$–40 μm.

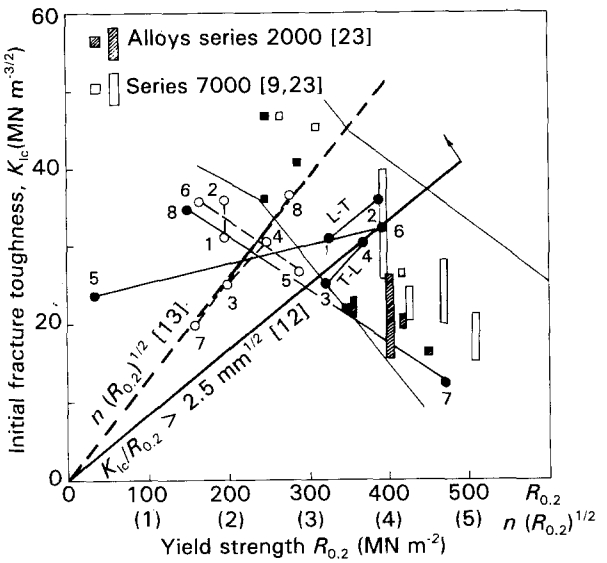

Figure 11 Comparison of K_{Ic} values for aluminium–lithium and values displayed by other high-strength alloys with fracture models of Hahn and Rosenfield for a hypothetical requirement $K_{Ic}/R_{0.2} \geq 2.5\ mm^{1/2}$ [12] and Garrett and Knott for $K_{Ic} \propto n(R_{0.2})^{1/2}$[13]. 1, T6-UA(L–T); 2, T6-PA(L–T); 3, T6-UA (T–L); 4, T6-PA(T–L). From Venkateswara Rao and Ritchie [9]: 5, 8090-T351; 6, 8090-T8X; 7, 8091-T8X; 8, 8091-T351.

the other commercial aluminium–lithium alloy [9, 11, 16], for aged microstructures and corresponding orientations. Ageing of alloy 8090 from the UA to PA temper leads to an increase in K_{Ic} with $R_{0.2}$, whereas the traditional alloys usually show a decrease of toughness after ageing to peak strength. Possible reasons for the superior strength and toughness properties shown by this pure alloy 8090 are related to limited grain-boundary precipitation of insoluble iron- and silicon-rich constituents, while in the PA condition of the alloy plates, S′-laths appear precipitated uniformly in the matrix of elongated grains. These S′-laths strengthen the plastic ligaments, increasing the possibility for cross slip. The uniform precipitation of S′ phase is promoted by prolonged natural ageing.

The ratio of total fracture R_0 impact and J_{Ic} static energies, R_0/J_{Ic}, is a function of orientation and heat treatment as shown in Table IV. The ratio of the UA specimens in the L–T orientation is higher by a factor of 2.5 compared to PA specimens of the T–L orientation. It is considered that the underaged material is more resistant to shock loading under high impact strain rates than the peak-aged one.

4. Fracture models

The trend of the initial fracture toughness change of aluminium alloys is generally interpreted by the application of theoretical models for ductile fracture [12, 13]. A number of attempts to relate the K_{Ic} to the yield strength, $R_{0.2}$, or fracture stress, R_f, and a characteristic microstructural dimension such as: size, nearest neighbour spacing of the void initiating particles, λ, a critical peak fracture strain, plastic zone, ε_c, or volume fraction of precipitates, have been reported [9, 13]. The most useful treatment for ductile fracture of high-strength aluminium alloys has been proposed by Hahn and Rosenfield [12]. They suggested a model of fibrous crack extension based on criteria of the critical crack-tip opening displacement, δ_c, exceeding the mean critical spacing of the void-initiating particles, λ_c, by way of Equation 1, or $J_{Ic} \approx R_{0.2}\lambda_c^*$, where λ_c^* is a local critical spacing of the void-initiating particles, by assuming that the local peak plastic zone of the heavily strained region at the crack tip is very small, ε_c^*. Then Equation 1 becomes

$$K_{Ic} \approx (E' R_{0.2} \lambda_c)^{1/2} \quad (3)$$

Equation 3 has a serious drawback in the constant of proportionality (length)$^{1/2}$. The model predicts an unusual trend: the increasing K_{Ic} as a simple product of the $R_{0.2}$ and an increase of λ_c.

Equation 3 can be adequately applied to the fracture process of 10 mm thick plate materials, by assuming that the λ_c^* is equal to the width of the local broken ligament, d_p^*, shown by arrows in Fig. 8a and b, separating two rows of the crack-initiating coarse β′, T and S particles, see Fig. 3b, closely distributed at a lower spacing along high-angle grain boundaries, λ_g ($\ll\lambda_c$), i.e. $\lambda_c^* \approx d_p^*$. The ligament width, d_p^*, is appropriate for predicting the fracture toughness and crack extension by failure of adjacent ligament followed by microvoid coalescence along high-angle grain boundaries. The deformation proceeds between two rows of inclusions remaining localized to the ligament. Fig. 8 illustrates the typical crack-divider fracture features of the PA material characterized by LLC formation along high-angle grain boundaries. In the early stages of LLC propagation, the extent of the heavily strained region at the crack tip is comparable to d_p, which is approximately equal to an average "pancake" grain thickness, d, measured along the short-transverse direction of plate, $d_p \approx d = 20$–40 μm (Figs 3, 5 and 8). For 10 mm thick plates ($\lambda_g \ll d_p$), the failure of ligament, d_p^* is definite proof that mechanism of fracture is, in fact, strain, transgranular shear $\approx 45°$ (shown in Fig. 8a) or intersubgranular (Fig. 8b) controlled. The plastic zone between two rows of inclusions approximated by the ligament width is calculated from Equation 3, i.e. $d_p \approx K_{Ic}^2/R_{0.2}E'$, using the experimental values in Tables II and IV. Calculated values of d_p are in good agreement with measured values and are found to be approximately the same for both heat-treated materials, they do not depend on ageing condition and for a fixed composition and fabrication practice (texture) of alloy they remain essentially constant. It is important to note that the calculated ligament width, d_p, depends only on the plate orientation. For a relatively high volume fraction of β′ dispersoids, including that of T and S particles, in this plate material the transgranular shear fracture region is low, critical values of δ_c also being much lower than for an alloy without dispersoids or plate material with higher total rolling reductions. In fact, by increasing the rolling reduction to 6 mm thick plates, particle spacing λ_g (along high-angle grain boundaries) increases to a critical value, λ_c, laminated cracks disappear and Equation 3 can no longer be applied to predict toughness. For 6 mm thick plates, rolling limits the final

ligament width to a value approximating to the average interparticle spacing, $\lambda_g \approx \lambda_c \approx d_p$ for $d_p \approx d = 10$–15 μm. The deformation extends over a larger volume of matrix, more work hardening occurs, and voids which nucleated at particular particles can grow to a size considerably in excess of the ligament width, d_p^*, without the interference of adjacent rows of particles. The fracture mechanism transforms to plane stress, slant fracture, at the critical plate thickness of the order of B_c, see Equation 2. The elongation to failure of tensile specimens (Table IV) increases with the appearance of triaxial stresses at the crack tip, i.e. local necking appears, see Curves (8) and (9) in Fig. 4. The effect of splitting on crack growth and toughness in 6 mm thick plates is relatively minimal. When plastic deformation by rolling proceeds to sheets 1.6 mm thick, laminated cracks are absent, the particle spacing, λ_g, increases considerably so that $\lambda_g \gg d_p$ and the plastic zone at the crack tip increases, to a large extent, ε^*. The elongation to failure in the L–T orientation of sheet specimens considerably decreases to 2%–3% [16, 17], due to strain localization across a sheet thickness. A few crack-initiating particles along high-angle grain boundaries enable slip planarity across a few rows of ligaments, because grain boundaries without particles represent a weak obstacle to moving dislocations (dislocation avalanche). In sheet forms (≤ 6 mm), the absence of such through-thickness delaminations permits completely plane stress deformation conditions. The crack-tip plasticity is sufficiently large (ε^*) to completely relieve constrain across a sheet thickness.

Conversely, Garrett and Knott [13] have adapted the critical strain criterion, given by Equation 3 by assuming that the peak plastic strain at the crack tip exceeds a critical strain ε_c^*. They suggest the expression

$$K_{Ic} \propto n(R_{0.2}\varepsilon_c^* E')^{1/2} \quad (4)$$

where n is the strain-hardening exponent, Table II. Comparison of fracture toughness for aluminium–lithium and values displayed by other high-strength alloys with the above fracture models, for a hypothetical requirement $K_{Ic}/R_{0.2} \geq 2.5\ \text{mm}^{1/2}$ and $K_{Ic} \propto n(R_{0.2})^{1/2}$, is shown in Fig. 11. The K_{Ic} in both orientations indicates different trends to the model's predictions, implying that a precise understanding of fracture mechanisms in these instances is far from complete. The K_{Ic} values of alloy 8090 with respect to ageing conditions (UA and PA) and both orientations agree well to the first model's prediction [12], except that for 8091 alloy, points 7 and 8 [9]. Hahn and Rosenfield's model is in better agreement with experimental results presented here, than is the model of Garrett and Knott.

Finally, it is important to note that, for a better toughening of the plates and sheets, it is of interest to decrease and strengthen the ligament, d_p^*, by introducing a large number of S′ laths precipitated on dislocation networks and, at the same time to increase the number of coarse particles between ligaments. For a lower ligament width (thin laminates), to be effective in toughening the through-thickness splits must be ascertained by a special thermo-mechanical treatment for the inclusion of weak interfaces in the microstructure, prior to initiation of the main crack. Producing a large number of thin strong ligaments would result in substantial toughening along specific orientations.

It appears that subgrain fracture is the more dangerous fracture mode in this aluminium–lithium alloy, i.e. it determines the toughness levels of the alloy.

5. Conclusions

The experimental results which show the influence of heat treatment and orientation on the mechanical properties of 8090 alloy lead to the following conclusions.

1. A very low strength of only 31.2 MPa and low elongation to failure were observed in as-cast slowly solidified material, $\approx 0.125\ \text{K s}^{-1}$, following final artificial ageing at 463 K, due to nearly complete precipitation of alloying element atoms in the grain matrix and at grain boundaries.

2. A critical thickness of the rolled product exists, $B_c \approx 0.16\ t_i$, where t_i is the starting thickness of the rolling ingot, for which the L–T tensile properties are the same as those in the T–L orientation, while the plasticity of the plate is maximal, for a constant dispersoid content and fabrication practice.

3. Not all specimen orientations show improved impact toughness at a cryogenic temperature of 77 K. The toughness of peak-aged specimens significantly increases in the L–T orientation and is attributed to freezing of sodium or potassium impurity atoms at subgrain boundaries and an increase in delamination toughening and enhanced ductility.

4. Two types of laminated cracks on the fracture surface of specimens were observed: large > 1 mm, the number of which is equal to the number of hot-rolling passes, and fine 0.1–0.4 mm, the number of fine cracks is two to three times greater at 77 K than at 293 K.

5. The ligament width, d_p^*, approximately equal to an average grain thickness, d, is appropriate for predicting the fracture of the laminated microstructures of alloy 8090. The d_p^* does not depend on ageing conditions but on the plate orientation, i.e. distribution of dispersoids along high-angle grain boundaries.

Acknowledgements

The authors thank Professor John W. Martin, University of Oxford, for helpful discussion and suggestions during the preparation of this paper. They also thank the Air Force Materials Laboratory and the Ministry of Defence, Belgrade, for the support of this work, under contract Pov. 2082-1-2-3. The experimental assistance of Mr M. Isailovich and Mr I. Djurich is also gratefully acknowledged.

References

1. T. H SANDERS Jr and E. A. STARKE Jr (eds), "Proceedings of the 1st International Conference on Al–Li Alloys I", Stone Mountain, Georgia, May 1980 (Metallurgical Society of AIME, Atlanta, 1981).

2. *Idem*, "Proceedings of the 2nd International Conference on Al–Li Alloy II", Monterey CA, May 1983 (Metallurgical Society of AIME, Warrendale, PA, 1984).
3. C. BAKER, P. J. GREGSON, S. J. HARRIS and C. J. PEEL (eds), "Proceedings of the 3rd International Conference on Al–Li Alloys III," Oxford, UK (Institute of Metals, London, 1986).
4. G. CHAMPIER, B. DUBOST, D. MIANNAY and L. SABETAY (eds), "Proceedings of the 4th International Conference on Al–Li Alloys IV," Paris, June 1987, Journal De Physique, Coll C3, Suppl. and No. 9, Vol 48, 1987.
5. T. H. SANDERS Jr and E. A. STARKE Jr (eds), "Proceedings of the 5th International Conference on Al–Li Alloys V," Williamsburgh, Virginia, March 1989.
6. T. S. SRIVATSAN and T. ALAN PLACE, *J. Mater. Sci.* **24** (1989) 1543.
7. E. J. LAVERNIA, T. S. SRIVATSAN and F. A. MOHAMED, *ibid.* **25** (1990) 1137.
8. T. KABAYASHI, M. NIINOMI and K. DEGAWA, *Mater. Sci. Technol.* **5** (1989) 1013.
9. K. T. VENKATESWARA RAO and R. O. RITCHIE, *ibid.* **5** (1989) 882.
10. *Idem*, *Acta Metall. Mater.* **38** (1990) 2309.
11. K. T. VENKATESWARA RAO, W. YU and R. O. RITCHIE, *Metal. Trans.* **20A** (1989) 485.
12. G. T. HAHN and A. R. ROSENFIELD, *ibid.* **6A** (1975) 653.
13. G. G. GARRETT and J. F. KNOTT, *ibid.* **9A** (1978) 1187.
14. V. M. STEFANOVIĆ, V. CVETIĆ, V. LUČIĆ and Lj. V. PIRIĆ, to be published.
15. X. XIAOXIN and J. W. MARTIN, *Mater. Sci. Eng.* **A128** (1990) 113.
16. N. GRAHOVAC, V. LUČIĆ, Z. BURZIĆ and V. M. STEFANOVIĆ, in Proceedings of the 35th Yugoslavian Conference ETAN", Ohrid, June 1991, Vol. 1B-14 (1991) p. 61.
17. K. WELPMANN, H. BUHL, R. BRAUN and M. PETERS, in "Proceedings of the 4th International Conference on Al–Li Alloys IV", edited by G. Champier, B. Dubost, D. Minnay and L. Sabetay, Journal de Physique, Coll. C3, Suppl. and no. 9, vol. 48, p. C3–677.
18. W. S. MILLER, J. WHITE and D. J. LLOYD, *ibid.*, p. C3–139.
19. D. WEBSTER, *Metall. Trans.* **18A** (1987) 2181.
20. J. GLAZER, S. L. VERZASCONI, R. R. SAWTELL and J. W. MORRIS, *ibid.* **A18A** (1987) 1686.
21. K. V. JATA and E. A. STARKE Jr, *Scripta Metall.* **22** (1989) 1553.
22. Y. B. XU, L. WANG, Y. ZHANG, Z. G. WANG and Q. Z. HU. *Metall. Trans.* **22A** (1991) 723.
23. R. DEVELAY, *Met. Mater.* **6** (1972) 404.

Received 29 September 1992
and accepted 3 February 1993